Programmed synthesis of three-dimensional tissues

Michael E Todhunter[1,2,8], Noel Y Jee[1,3,8], Alex J Hughes[1], Maxwell C Coyle[1], Alec Cerchiari[1,4,5], Justin Farlow[1,2], James C Garbe[1,6], Mark A LaBarge[6], Tejal A Desai[3–5] & Zev J Gartner[1–3,5,7]

Reconstituting tissues from their cellular building blocks facilitates the modeling of morphogenesis, homeostasis and disease *in vitro*. Here we describe DNA-programmed assembly of cells (DPAC), a method to reconstitute the multicellular organization of organoid-like tissues having programmed size, shape, composition and spatial heterogeneity. DPAC uses dissociated cells that are chemically functionalized with degradable oligonucleotide 'Velcro', allowing rapid, specific and reversible cell adhesion to other surfaces coated with complementary DNA sequences. DNA-patterned substrates function as removable and adhesive templates, and layer-by-layer DNA-programmed assembly builds arrays of tissues into the third dimension above the template. DNase releases completed arrays of organoid-like microtissues from the template concomitant with full embedding in a variety of extracellular matrix (ECM) gels. DPAC positions subpopulations of cells with single-cell spatial resolution and generates cultures several centimeters long. We used DPAC to explore the impact of ECM composition, heterotypic cell-cell interactions and patterns of signaling heterogeneity on collective cell behaviors.

The functional properties of tissues arise through interactions of numerous cell types[1]. *In vivo*, these interactions occur in a three-dimensional (3D) setting in the context of specific tissue structures. Tissue structure—defined here as tissue size, shape, composition and spatial heterogeneity (i.e., the relative location of multiple cell types) and the surrounding ECM—serves to organize the exchange of chemical, electrical and mechanical information between neighboring and distant cells. An orderly exchange of signals allows cells to arrive at collective decisions and organize collective behaviors[2]. Defining the impact of a tissue's structure on the behavior of its constituent cells remains a major goal of developmental biology and is a requirement for the successful application of tissue engineering to regenerative medicine[3]. However, directly connecting tissue structure to collective cell behaviors remains challenging: tissue structure is difficult to alter *in vivo*, and the inherent structural complexity of tissues has so far precluded their *de novo* synthesis *in vitro*.

Current efforts typically focus on the narrower challenge of reconstituting specific elements of tissue structure *in vitro*. Common to all efforts is 3D cell culture, a requirement for proper tissue structure formation and cell behavior[4]. For example, 3D culture in mechanically and chemically defined ECM gels directs the morphogenesis of stem cells and cancer cells into organoids that model normal development and tumorigenesis, respectively[5–7]. However, rudimentary 3D culture methods lack key microenvironmental cues from surrounding tissue components that are necessary to specify tissue architecture over larger distances. Therefore, they provide limited control over ultimate tissue architecture. Dielectrophoretic patterning and micromolding have shown the effect of tissue size and shape on cell anabolic activity, differentiation, autocrine signaling, mechanics and tissue outgrowth[8–10]. However, dielectrophoresis is limited to conditions with low ionic strength, and micromolding cannot typically position multiple cell types in precise arrangements or use ECM formulations having physiological stiffness (<10 kPa), such as Matrigel. A variety of techniques have demonstrated that tissue composition, often referred to as cellular heterogeneity, contributes to a spectrum of collective cell behaviors absent from homogeneous tissues[11–13]. Finally, 3D printing techniques provide a potentially general strategy to reconstitute spatial heterogeneity for tissues with large features but suffer from low cell viability, can be limited in their ECM compatibility, and cannot efficiently build cell-dense tissues with spatial features the size of single cells[14]. Therefore, no generalizable methods are available for simultaneously reconstituting the size, shape, composition and spatial heterogeneity of tissues for long-term 3D culture.

To provide a rapid and modular means of reconstituting multiple aspects of tissue structure in 3D culture, we describe a bottom-up strategy that uses a DNA-patterned substrate[15] as a template and temporary DNA-based cellular adhesions[16–19] as synthetic linkages between cellular building blocks (**Fig. 1a,b**). DPAC is a modular method for controlling 3D microtissue structure across multiple length scales that can incorporate multiple cell types with high viability. We applied DPAC to study the impact of tissue size, shape, composition

and spatial heterogeneity as well as the embedding ECM on individual and collective cell behaviors.

RESULTS

To assemble an array of epithelial microtissues embedded in ECM gels, we proceeded through a series of steps (**Fig. 1c** and **Supplementary Video 1**) that begin with patterning a series of ~7-μm amino-modified DNA spots on an aldehyde-coated glass slide using a BioForce Nano eNabler[20,21]. Reductive amination results in a covalent linkage between the DNA and the slide. A 180-μm-tall poly(dimethylsiloxane) (PDMS) flow cell was placed above the DNA pattern, allowing the addition of reagents and cell suspensions in a minimized (30-μl) volume. The slide was passivated to background cell binding by treatment with hydrophobic silane and blocking with albumin. In parallel, two populations of human mammary epithelial cells (MCF10A) were labeled for 5 min with a 5 μM solution of either a lipid-modified oligonucleotide or its complement[17,22]. The cells labeled with DNA complementary to the template were introduced to the flow cell and incubated for 5 min. Single cells adhered to single DNA spots. After gentle washing, a pattern of cells matching the pattern of DNA spots on the template was revealed. Iterating with alternating populations of complementarily labeled cells assembled hemispherical microtissues, layer-by-layer, upward and outward from the single cells (**Supplementary Fig. 1**). Addition of Matrigel containing DNase cleaved the DNA, releasing the array of microtissues into the supporting ECM gel as it set at 37 °C. Finally, the gel-encapsulated array was removed from the surface template, and an underlay of liquid ECM gel resulted in a seamless and fully embedded 3D culture upon gelation.

To more clearly illustrate the 3D embedding process, we assembled microtissue arrays through two rounds of DPAC but embedded the arrays in Matrigel containing covalently bound Alexa Fluor 555 and then underlaid the arrays with Matrigel containing Alexa Fluor 488. The unstained microtissues were observed at the interface of the two fluorescent gel layers. No voids were observed. The initially DNA-adherent cells were found to concentrate the gels at their surfaces over 24 h in culture as they rearranged and condensed into microtissues (**Fig. 1d**). Cell viability exceeded 97% (n = 613) through assembly, transfer to ECM gels and 24-h culture. Microtissues polarized their cytoskeletal and adhesion machinery appropriately, consistent with previous reports[11,23] (**Supplementary Fig. 1**).

Precise DNA surface patterning provides the opportunity for precise spatial arrangement of large numbers of single cells, and whole microtissues, for fully embedded 3D culture. To quantify the capacity of DPAC to preserve spatial information when transferring patterns of cells from two dimensions to three dimensions, we first prepared arrays of DNA triangles with 18-μm or 38-μm edges. We used DPAC to render the DNA pattern as cells fully embedded in a Matrigel slab. Imaging of the embedded culture revealed a cell-to-cell spacing of 20 ± 2 and 40 ± 3 μm, respectively (mean ± s.d., n = 400; **Fig. 2a** and **Supplementary Fig. 2**). In another experiment, we varied cell spacing between two cell types in increments of several micrometers (**Supplementary Fig. 3**). To quantify the precision of cell positioning over larger distances and in less repetitive and more biologically inspired arrangements, we generated a bitmap pattern from a whole mount image of a mouse mammary fat pad. We used DPAC to render the image as a 1.6-cm pattern of over 6,000 single mammary epithelial cells fully embedded in Matrigel (**Fig. 2b**). The difference between cell positions on glass (2D) and embedded in Matrigel (3D) were visualized using a heat map (**Fig. 2c,d**). The majority of the differences occurred along the long, open axis of the flow cell (**Supplementary Fig. 2**). Expected cell-cell distances differed from actual cell-cell distances with a median of

Figure 1 | Programming the reconstitution of fully ECM-embedded 3D microtissue arrays by DNA-programmed assembly (DPAC). (**a**) Scheme showing the relationship between DNA spots (colored squares), DNA-programmed connectivity (colored lines) and multistep assembly. (**b**) Incubation of cells with lipid-modified oligonucleotides results in chemical remodeling of cell surfaces. Combining cells bearing complementary cell-surface oligonucleotides forms a temporary chemical adhesion. (**c**) 7-μm amino-modified DNA spots are patterned onto aldehyde-coated glass slides and covalently linked to the surface by reductive amination. Cells bearing complementary cell-surface oligonucleotides are introduced above the patterned substrate at high concentration and at controlled flow rate using a flow cell. Cells adhere to the appropriate DNA spot, and excess cells are removed by gentle washing. Iteration of this process assembles the microtissue into the third dimension. Addition of liquid ECM incorporating

DNase releases the assembled microtissues from the template; they are trapped in the embedding ECM as it gels. The gel is peeled off the glass, releasing the tissues. Underlay of the gel with additional ECM results in a fully embedded 3D culture. Cells interact with each other and their microenvironment as they condense into 3D microtissues. (**d**) DPAC using MCF10A mammary epithelial cells showing (i) DNA spots, (ii) cells in a flow cell and (iii) a single-cell array followed by additional rounds of programmed assembly. *xz* reconstructions show an unstained MCF10A cell aggregate embedded between Alexa Fluor 488– and Alexa Fluor 555–stained layers of Matrigel at 0 (iv) and 24 h (v). Scale bars, 100 μm.
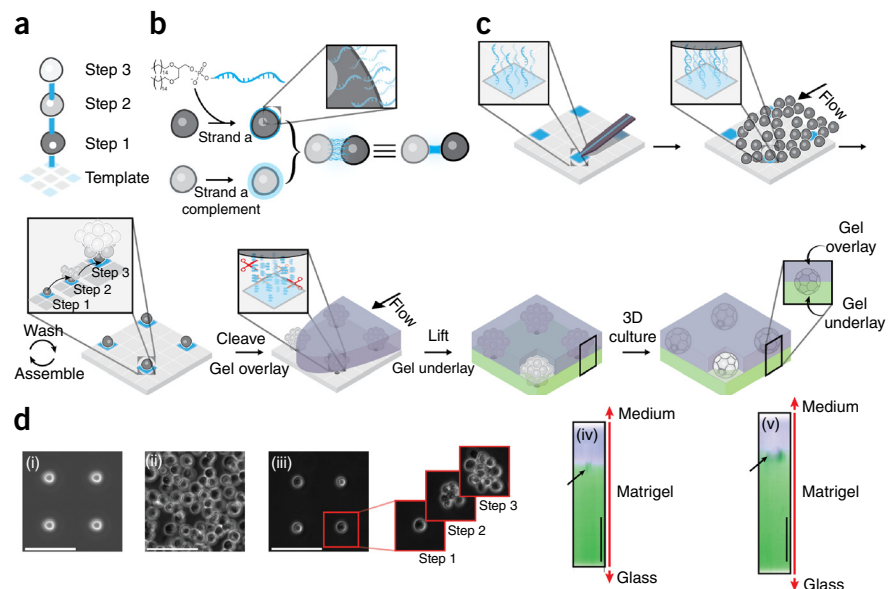
Figure 2 | Cell position is preserved upon transfer of cell patterns from their 2D template to fully embedded 3D culture. (**a**) Matrigel-embedded cell triangles having a nominal cell-to-cell spacing of 18 and 38 μm. (**b**) A whole-mount image of a mouse mammary fat pad (reproduced with permission of W. Muller) was digitized, used to print a pattern of DNA spots, and rendered as a 1.6-cm-long pattern of single cells fully embedded in Matrigel. (**c**) Globally aligned and superimposed images of the cell pattern while still attached to the glass template (green) and fully embedded in Matrigel (magenta). Global and relative differences in cell positioning were calculated using the indicated metrics. (**d**) Heat map illustrating differences in global cell position in two dimensions vs. three dimensions relative to the pattern center. (**e**) Graph generated from over 36 million cell pairs relating the difference from expected cell-to-cell distances for the pattern in **b**. (**f**) Histogram showing deviations from expected cell-to-cell distances for all cell pairs patterned within 50 μm of one another. Scale bars, 100 μm.

22 μm across the whole pattern ($n = 3.6 \times 10^7$ pairs) (**Fig. 2e**) and only 10 μm across cell pairs spaced less than 50 μm apart ($n = 1.9 \times 10^4$ pairs) (**Fig. 2f**).

We found that DPAC is compatible with varied cell types and ECMs. Because cellular interactions are programmed with DNA, rather than genetically encoded adhesion molecules, the identity of the feedstock cells is arbitrary. For example, we successfully patterned primary or immortalized neuronal, epithelial, fibroblastic, endothelial and lymphocytic cells with high resolution and yield (**Supplementary Fig. 1**). The choice of matrices is limited only by what can be added to the cellular pattern as a liquid and subsequently gel under biocompatible conditions. Thus, we transferred patterns of cells to Matrigel, collagen, fibrin, agarose and their mixtures (**Supplementary Fig. 1**).

We also found that DPAC provides a flexible strategy for simultaneously controlling tissue size, shape, composition, spatial heterogeneity and ECM. We first demonstrated simultaneous control of tissue size and composition by showing that pairs of green and red fluorescent epithelial cells patterned closer than 18 μm apart condensed into single tissues upon transfer to Matrigel (**Supplementary Fig. 3**). Triangles comprising three uniquely stained epithelial cells behaved similarly (**Fig. 3a**). We prepared microtissues of equivalent size but different composition by performing multistep DPAC on cell triangles having two possible compositions (**Fig. 3b,c**). We prepared an array of over 700 microtissues containing a target of 8–13 cells total but either one or three fluorescent cells. For both compositions, 85% of microtissues contained the target number of total cells, and 79% of those microtissues also contained the target number of fluorescent cells. In comparison, the theoretical maximum yield for a Poisson-limited method, such as microwell molding, would be 26% or 16% for one or three fluorescent cells, respectively. We prepared larger microtissues by either increasing the area of the templating DNA pattern or further iterating layer-by-layer DPAC (**Fig. 3d** and **Supplementary Table 1**).

A unique capability of DPAC is its capacity to reconstitute cell-dense microtissues having tailored spatial heterogeneity. Unlike a printer, DPAC defines cell position by cell-cell connectivity rather than coordinates in a 3D Euclidean space. Therefore, the templating DNA pattern, and the order of addition of different DNA-functionalized populations of cells, determines the cell-cell connectivity of the assembled microtissue. To demonstrate this concept, we used DPAC to reconstitute microtissues consisting of three juxtaposed cellular compartments, with one compartment
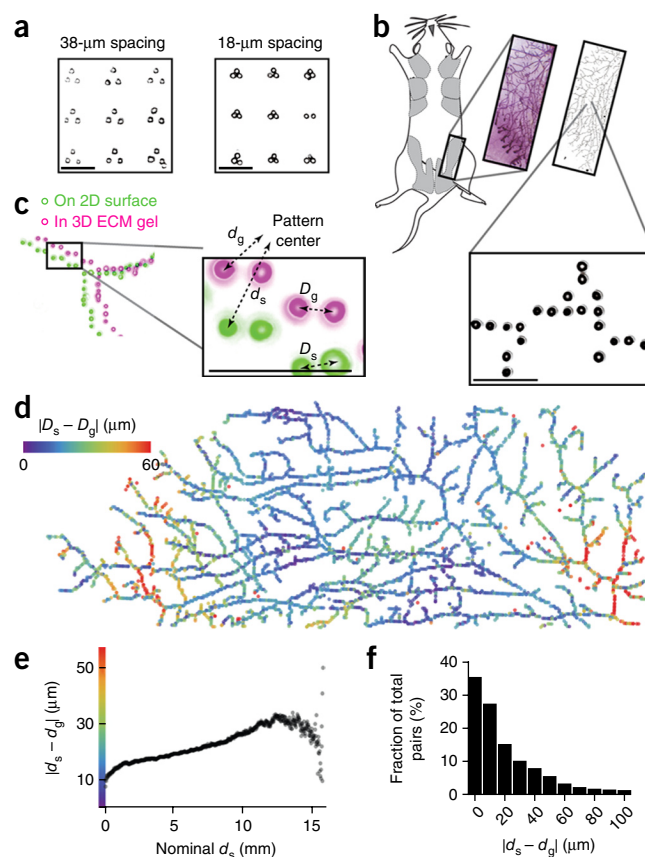
boundary in the *xy* plane and the other in the *xz* plane (**Fig. 3e**). This was accomplished using two orthogonal pairs of DNA sequences and a specific eight-step assembly scheme. We elaborated this strategy to form a microtissue having a core-shell topology similar to that of the human mammary gland. We assembled primary human luminal (LEP) and myoepithelial (MEP) cells using two orthogonal DNA sequences, a six-step DPAC scheme and a bull's eye–shaped templating pattern. When released from the template and fully embedded in Matrigel, the microtissue retained the programmed topology, which was reinforced after 24 h in culture (**Fig. 3f**). Some of these microtissues had lumenized by 72 h (**Supplementary Fig. 3**). We used a similar strategy to prepare arrays of either homogeneous or heterogeneous filled tubes of MCF10A cells having defined patterns of spatial heterogeneity (**Fig. 3g,h**).

DPAC provides a means to elucidate the effects of tissue structure on collective cell behavior by allowing simultaneous control of tissue size, shape, composition and spatial heterogeneity and the surrounding ECM. We explored this enabling capacity of DPAC in several model systems.

We first explored the impact of ECM composition on organoid tissue branching. We assembled microtissues from primary human luminal and myoepithelial cells; these microtissues were then embedded in either Matrigel or collagen I. Collagen I has previously been shown to influence the branching of mouse mammary organoids. Such organoids are prepared by mincing intact tissues, which yields a wide distribution of sizes and shapes[24]. To control for size and shape, we used DPAC to assemble similarly sized microtissues that were initially round upon transfer to Matrigel or collagen (**Fig. 4a**). After 24 h of culture, collagen-embedded microtissues had lower circularity (mean ± s.d. of
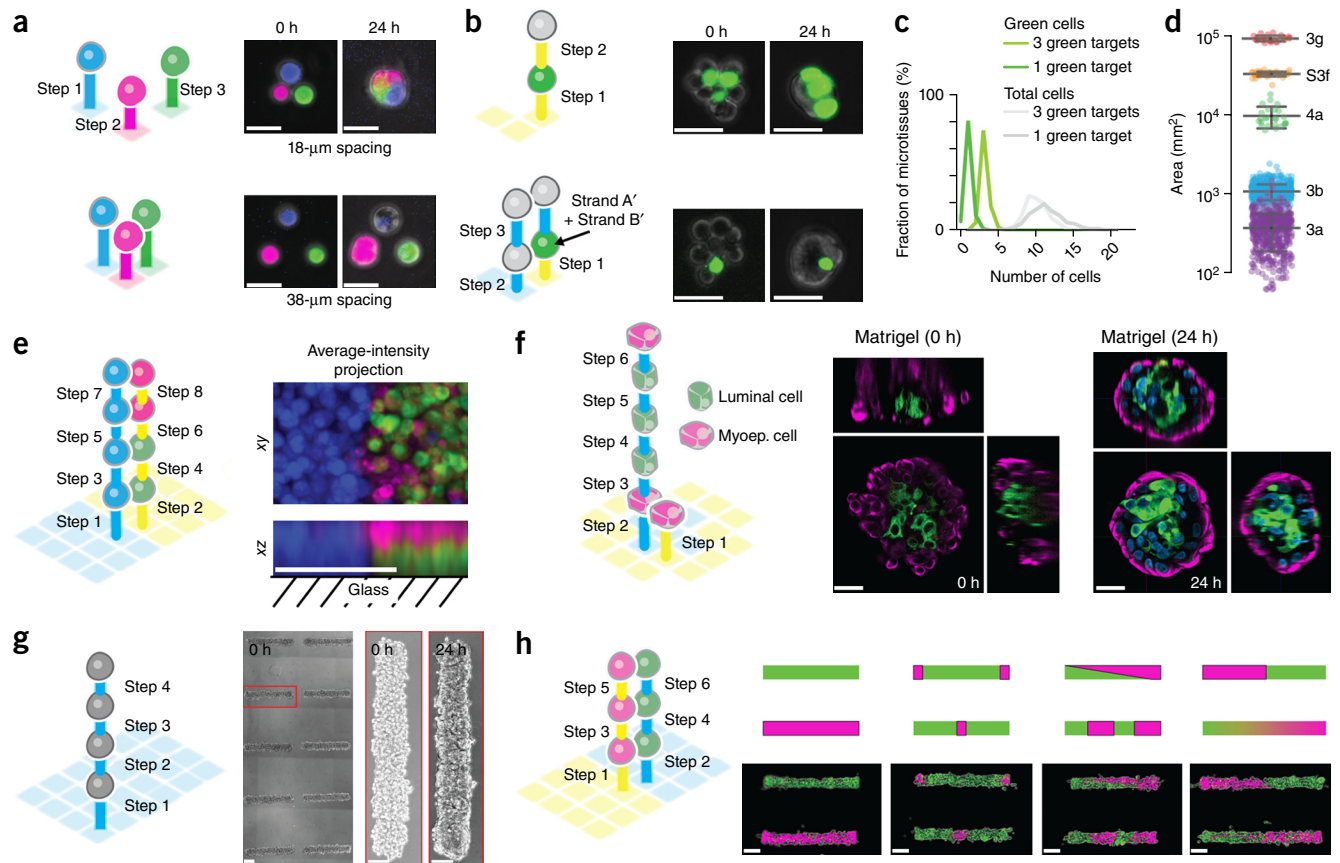
Figure 3 | Reconstituting epithelial microtissues with programmed size, shape, composition, spatial heterogeneity and embedding ECM. (**a**) Scheme and images of magenta-, green- and blue-stained MCF10A cells patterned with 18- and 38-µm spacing and fully embedded in Matrigel. (**b**) Scheme and images for Matrigel-embedded MCF10A microtissues programmed with two distinct compositions (one or three green cells) but similar average sizes. (**c**) Quantification of microtissue composition for data in **b**. (**d**) Distribution of cross-sectional areas (mean ± s.d.) for microtissues assembled through each of five synthetic schemes (**Supplementary Table 1**; 3a, $n = 507$; 3b, $n = 640$; 4a, $n = 25$; S3f, $n = 40$; 3g, $n = 25$). Note that purple features (3a) come from single-cell arrays, included to indicate the fundamental heterogeneity in the sizes of the cellular building blocks. (**e**) Scheme and average-intensity projections for a multicellular assembly having three mutually perpendicular cell compartments. (**f**) Scheme and images of fully embedded aggregates of human luminal and myoepithelial cells. (**g**) Four-step synthetic scheme and images of MCF10A cells assembled into cylindrical microtissues and transferred to Matrigel-collagen mixtures. Images of cells show a zoomed-out view (left), a zoomed-in view (center) and a zoomed-in view after 24 h of growth (right). (**h**) Scheme, diagram and images of cylindrical microtissues having defined patterns of spatial heterogeneity. Scale bars: 30 µm (**a**,**b**,**f**) and 100 µm (**e**,**g**,**h**).

0.36 ± 0.13, $n = 25$) than Matrigel-embedded microtissues (mean ± s.d. of 0.73 ± 0.11, $n = 25$, $P = 2.8 \times 10^{-14}$, two-tailed Welch's t-test) (**Fig. 4a**,**b**). Qualitatively, the pattern of branching in collagen resembled those previously reported for randomly minced mouse mammary organoids[24].

We next explored the impact of tissue size on cell growth rate. We reconstituted over 1,000 MCF10A (10A) microtissues ranging in size from 2 to 20 cells and tracked cell position over 72 h. Analysis of the growth trajectories of individual microtissues revealed that growth rate was inversely proportional to initial microtissue size. This trend was also observed for microtissues assembled from more rapidly dividing cells expressing oncogenic H-Ras^{V12} (10AT), as well as for microtissues bearing mixed populations of 10As and 10ATs (**Fig. 4d** and **Supplementary Fig. 4**). Proliferation rates fit a generalized logistic growth model[25].

We next explored the impact of tissue composition on the growth of single cells, but in microtissues of fixed size. We synthesized an array of 5- to 8-cell microtissues from mixed populations of 10As and 10ATs (**Fig. 4c**). As expected, microtissues grew more rapidly as the proportion of 10ATs in the tissue increased (**Fig. 4d**).

Unexpectedly, the rate of microtissue growth did not appear to be a linear combination of the growth rates of the two cell populations. Further investigation revealed that 10ATs triggered a statistically significant increase in the growth rate of neighboring 10As (**Fig. 4e**) (mean 0.53×10^{-2} h^{-1}, $P = 0.04$, one-way analysis of variance (ANOVA) with Holm-Sidak correction). Intriguingly, this effect appeared to require more than one 10AT cell in the tissue ($P = 0.03$, one-way ANOVA with Holm-Sidak correction) (**Supplementary Fig. 4**), suggesting that even small compositional differences can alter the rate of tissue growth through cell-cell interactions.

Finally, we explored the impact of defined spatial heterogeneity on branching morphogenesis. During the branching morphogenesis of a variety of tissues, gradients of growth factors trigger the activation of their receptors and downstream pathways in distinct patterns of spatial heterogeneity[26–29]. Whether the heterogeneous patterns of pathway activation are sufficient to trigger branching tissue outgrowth—or whether additional guidance cues from external gradients are required—has not been explored. Therefore, we used DPAC to synthesize filled tubes of 10As incorporating
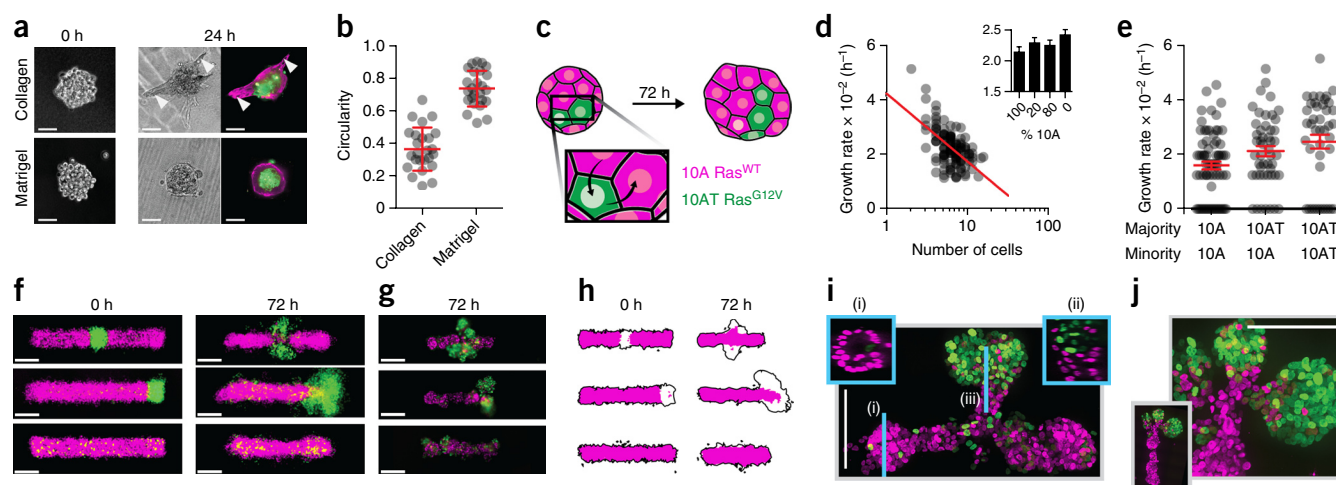
Figure 4 | Measuring the impact of microtissue size, shape, composition and spatial heterogeneity and the embedding ECM on collective cell behaviors. (**a**) Representative images of human mammary luminal and myoepithelial cells assembled through identical four-step synthetic schemes and then transferred to Matrigel or collagen I. (**b**) Quantification (mean ± s.d.) of microtissue morphology for the experiment in **a** (*n* = 25 for both conditions). (**c**) Scheme for assessing the impact of composition on the growth rate of 10A and H-Ras^{G12V}–expressing 10AT cells. (**d**) Effect of initial microtissue size on cell growth rate for 10As (*n* = 123). Inset shows growth rate (mean ± s.d.) for microtissues having different compositions. (**e**) Growth rates (mean ± s.d.) of single cells (minority) cultured in microtissues having the indicated majority cell type (*n* = 71, 49, 42). (**f**) Average-intensity projections of 12–14 single confocal sections of 10As (magenta = H2B-mCherry) and 10ATs (green = H2B-EGFP) in Matrigel-collagen mixtures. (**g**) Representative epifluorescence microscopy images of microtissue after 72 h of culture. (**h**) 90% intensity contours of the collection of microtissues from **f**. The black outline is the contour of the entire microtissue, and the magenta region is specifically the 10A component. (**i**) Maximum-intensity projection of a center-patterned microtissue after processing using CLARITY. Insets are single confocal sections of the indicated region of the microtissue. (**j**) Maximum-intensity projection showing detail from the branching region of an end-patterned tissue (inset) after processing using CLARITY. Scale bars, 100 μm.

10% 10ATs. As 10ATs express the Ras oncogene at low levels, they simulate a population of cells with chronic stimulation of their growth factor receptors[11]. The 10ATs were patterned randomly, in the middle or at the end of the 10A-filled tubes.

Cell dynamics and tissue morphology differed substantially between the three patterns over 72 h. We visualized changes in microtissue morphology by capturing single confocal slices from at least 12 microtissues from each cell pattern, which were combined to generate average intensity maps of the fluorescent 10A and 10AT nuclei (**Fig. 4f**). 10ATs in randomly patterned tubes comingled with 10As but also extruded basally or capped local protrusions, consistent with previous reports[11,30] (**Fig. 4f,g** and

Supplementary Fig. 4). However, 10ATs patterned in the middle of tubes translated outward laterally and formed filled acini-like structures. Similar results were observed for tubes incorporating 10% 10ATs at their ends. Branching occurred along all three axes (**Supplementary Fig. 4**). End-patterned microtissues showed a statistically significant increase in length at 72 h (mean ± s.d. of 371 ± 38 μm, *n* = 18, *P* = 7.6 × 10^{-6}, two-tailed Welch's *t*-test) compared to microtissues in which the 10ATs were patterned in the center (mean ± s.d. of 319 ± 28 μm, *n* = 18). 90% intensity contours of 14 tissues indicated that the 10A component was also substantially longer in these tissues compared to the microtissues having 10ATs patterned centrally or randomly (**Fig. 4h**). We examined the 3D structure of these microtissues qualitatively
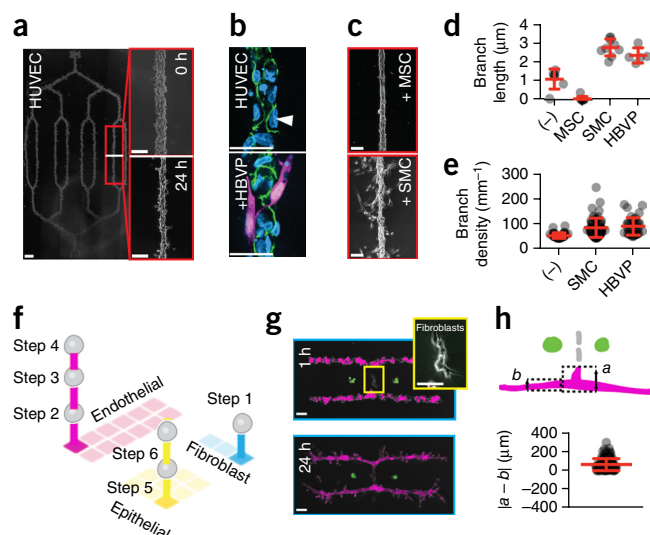
Figure 5 | DPAC control of stromal architecture. (**a**) HUVEC cells assembled (scheme in **Fig. 3h**) into a 6.2-mm (corner-to-corner) network fully embedded in a Matrigel-collagen mixture. Detail shows the pattern immediately after transfer to gel and the same region after 24 h of culture. (**b**) Top, localization of VE-cadherin (green) at cell-cell interfaces and exclusion from cell-ECM interfaces (white arrowhead) in HUVEC networks. Bottom, HUVEC networks incorporating peripheral pericytes (HBVP, magenta). (**c**) Morphology of HUVEC networks assembled with the indicated accessory cell type and cultured for 24 h in a Matrigel-collagen mixture. MSC, mesenchymal stem cells; SMC, smooth muscle cells. (**d**,**e**) Quantification of branch length (mean ± s.d.; *n* = 7, 9, 9, 5) (**d**) and branch density (mean ± s.d.; *n* = 36, 59, 36) (**e**) in HUVEC networks incorporating the indicated accessory cell type. (**f**) Scheme for the assembly of a three-component microtissue incorporating epithelial and stromal cell types. (**g**) 3D tissue culture and detail of patterns containing perpendicularly oriented HUVEC networks and fibroblasts. (**h**) Analytical scheme and quantification (mean ± s.d.) of HUVEC extension in microtissues with HUVEC and fibroblast components (*n* = 110). Scale bars: 100 μm (**a**–**c**) and 500 μm (**g**).

by CLARITY[31] (**Fig. 4i,j** and **Supplementary Fig. 4**). 10As formed necks connecting the filled 10AT-containing acini to the main 10A microtissue. Middle- and end-patterned microtissues showed evidence of lumenization.

In vivo, epithelial tissues are supported by a variety of stromal cells, including fibroblasts, adipocytes, lymphocytes and endothelial cells. Therefore, we explored the capacity of DPAC to reconstitute stromal cells into spatially organized 3D cultures. First, we prepared a branched pattern of endothelial cells (HUVECs) 5 mm long and fully embedded in a Matrigel-collagen mixture. After 24 h, the pattern condensed into a continuous network of endothelial cells and formed side branches (**Fig. 5a** and **Supplementary Fig. 5**). Immunofluorescence staining of fixed 72-h cultures provided evidence of phenotypic maturity, including vascular endothelial cadherin (VE-cadherin) localization to cell-cell junctions and exclusion from cell-ECM interfaces (**Fig. 5b**). To more closely mimic vasculature, we prepared microtissues of HUVECs with human brain vascular pericytes (HBVPs). At 72 h, immunofluorescence staining revealed a subset of HBVPs stably associated with the HUVECs and extending cellular processes among endothelial cell-cell junctions[32] (**Fig. 5b**).

Second, we explored the impact of mural cells on the frequency and length of HUVEC side branches (**Fig. 5c–e**). After 24 h of culture, HUVECs branched with a frequency of 1.1 mm^{-1} (s.d. = 0.53, $n = 7$) and an average branch length of 58 μm (s.d. = 11 μm, $n = 36$) (**Fig. 5a,d,e**). Smooth muscle cells (SMCs) or HBVPs significantly increased the frequency (mean ± s.d. of $2.7 ± 0.4$ mm^{-1}, $n = 9$, $P = 0.0017$, two-tailed Welch's *t*-test, and mean ± s.d. of $2.3 ± 0.4$ mm^{-1}, $n = 5$, $P = 0.0009$, two-tailed Welch's *t*-test, for SMCs and HBVPs, respectively) (**Fig. 5d**) and the length (mean ± s.d. $89 ± 38$ μm, $n = 59$, $P < 0.0001$, two-tailed Welch's *t*-test, and mean ± s.d. $94 ± 35$ μm, $n = 36$, $P < 0.0001$, two-tailed Welch's *t*-test) of HUVEC side branches (**Fig. 5e**) when assembled superficially to the HUVEC cords. Mesenchymal stem cells (MSCs) decreased the frequency of side branches (mean of 0.041 mm^{-1}, $n = 9$, $P < 0.0001$, two-tailed Welch's *t*-test), yielding endothelial networks with remarkably smooth edges (**Fig. 5c,e**).

Finally, we generated a variety of microtissues having multiple and distinct epithelial and stromal compartments. These microtissues incorporated endothelial networks, fibroblasts and epithelial cells using six-step DPAC and three orthogonal pairs of DNA sequences (**Fig. 5f,g** and **Supplementary Fig. 5**). After 48 h of culture in Matrigel-collagen mixtures, some microtissues with perpendicularly oriented fibroblasts and HUVEC compartments distorted, with HUVECs forming extensions proximal to the patterned fibroblasts (**Fig. 5g**). We resynthesized microtissue arrays consisting only of correspondingly oriented fibroblasts and HUVECs and measured increased extension of HUVECs into ECM near (mean ± s.d. of $103 ± 47$ μm, $n = 106$) and far (mean ± s.d. of $85 ± 38$ μm, $n = 106$, $P = 1.4 × 10^{-3}$, one-tailed Welch's *t*-test) relative to the fibroblast compartment after 24 h of culture (**Fig. 5h**). These results demonstrate that the morphologies and behaviors of endothelial networks are altered by the proximity of networks of fibroblasts.

DISCUSSION

There remain numerous opportunities for improving DPAC. For example, delivery of structured chemical, physical and hemodynamic signals to assembled microtissues, as well as the potential to perfuse embedded vasculature, could be achieved by merging DPAC with microfluidic technologies such as those used in organs-on-a-chip[33]. Merging DPAC with 3D printing could provide a means to control the spatial heterogeneity of ECM in addition to the spatial heterogeneity of cells. Combined with DPAC, folding, stacking[34] or rolling[35] techniques could generate thicker microtissues. Finally, the incorporation of stem cells or even whole tissue fragments as building blocks could enable the study of organoid development and disease processes in higher throughput and in a more reproducible 3D setting[1]. However, DPAC is fundamentally limited to cells or tissue components that can survive dissociation and that can be labeled by DNA. Given the capacity of DPAC to directly link complex tissue structural features with specific single and collective cell behaviors, we anticipate that this method will find utility in a variety of contexts, both basic and applied.

METHODS

Methods and any associated references are available in the online version of the paper.

Note: Any Supplementary Information and Source Data files are available in the online version of the paper.

AUTHOR CONTRIBUTIONS

Z.J.G., N.Y.J. and M.E.T. conceived the study; Z.J.G., M.E.T., N.Y.J., M.C.C. and A.J.H. designed experiments; N.Y.J., M.E.T., A.C., A.J.H., M.C.C. and J.C.G. performed experiments; M.E.T., N.Y.J., M.C.C., A.J.H. and J.F. analyzed and interpreted the data; and Z.J.G., M.E.T., N.Y.J., M.C.C. and A.J.H. wrote the manuscript. M.A.L. and T.A.D. discussed and commented on the manuscript along with all other authors.

COMPETING FINANCIAL INTERESTS

The authors declare competing financial interests: details are available in the online version of the paper.

Reprints and permissions information is available online at http://www.nature.com/reprints/index.html.

1. Sasai, Y. Cytosystems dynamics in self-organization of tissue architecture. *Nature* **493**, 318–326 (2013).
2. Nelson, C.M. & Bissell, M.J. Of extracellular matrix, scaffolds, and signaling: tissue architecture regulates development, homeostasis, and cancer. *Annu. Rev. Cell Dev. Biol.* **22**, 287–309 (2006).
3. Bissell, M.J., Rizki, A. & Mian, I.S. Tissue architecture: the ultimate regulator of breast epithelial function. *Curr. Opin. Cell Biol.* **15**, 753–762 (2003).
4. Schmeichel, K.L. & Bissell, M.J. Modeling tissue-specific signaling and organ function in three dimensions. *J. Cell Sci.* **116**, 2377–2388 (2003).
5. Lancaster, M.A. & Knoblich, J.A. Organogenesis in a dish: modeling development and disease using organoid technologies. *Science* **345**, 1247125 (2014).

6. van de Wetering, M. *et al*. Prospective derivation of a living organoid biobank of colorectal cancer patients. *Cell* **161**, 933–945 (2015).
7. Shamir, E.R. & Ewald, A.J. Three-dimensional organotypic culture: experimental models of mammalian biology and disease. *Nat. Rev. Mol. Cell Biol.* **15**, 647–664 (2014).
8. Albrecht, D.R., Underhill, G.H., Wassermann, T.B., Sah, R.L. & Bhatia, S.N. Probing the role of multicellular organization in three-dimensional microenvironments. *Nat. Methods* **3**, 369–375 (2006).
9. Nelson, C.M., Vanduijn, M.M., Inman, J.L., Fletcher, D.A. & Bissell, M.J. Tissue geometry determines sites of mammary branching morphogenesis in organotypic cultures. *Science* **314**, 298–300 (2006).
10. Stevens, K.R. *et al*. InVERT molding for scalable control of tissue microarchitecture. *Nat. Commun.* **4**, 1847 (2013).
11. Liu, J.S., Farlow, J.T., Paulson, A.K., LaBarge, M.A. & Gartner, Z.J. Programmed cell-to-cell variability in Ras activity triggers emergent behaviors during mammary epithelial morphogenesis. *Cell Rep.* **2**, 1461–1470 (2012).
12. Leung, C.T. & Brugge, J.S. Outgrowth of single oncogene-expressing cells from suppressive epithelial environments. *Nature* **482**, 410–413 (2012).
13. Boghaert, E. *et al*. Host epithelial geometry regulates breast cancer cell invasiveness. *Proc. Natl. Acad. Sci. USA* **109**, 19632–19637 (2012).
14. Murphy, S.V. & Atala, A. 3D bioprinting of tissues and organs. *Nat. Biotechnol.* **32**, 773–785 (2014).
15. Hsiao, S.C. *et al*. Direct cell surface modification with DNA for the capture of primary cells and the investigation of myotube formation on defined patterns. *Langmuir* **25**, 6985–6991 (2009).
16. Gartner, Z.J. & Bertozzi, C.R. Programmed assembly of 3-dimensional microtissues with defined cellular connectivity. *Proc. Natl. Acad. Sci. USA* **106**, 4606–4610 (2009).
17. Selden, N.S. *et al*. Chemically programmed cell adhesion with membrane-anchored oligonucleotides. *J. Am. Chem. Soc.* **134**, 765–768 (2012).
18. Bailey, R.C., Kwong, G.A., Radu, C.G., Witte, O.N. & Heath, J.R. DNA-encoded antibody libraries: a unified platform for multiplexed cell sorting and detection of genes and proteins. *J. Am. Chem. Soc.* **129**, 1959–1967 (2007).
19. Teramura, Y., Chen, H. & Kawamoto, T. Control of cell attachment through polyDNA hybridization. *Biomaterials* **31**, 2229–2235 (2010).
20. Birch, H.M. & Clayton, J. Cell biology: close-up on cell biology. *Nature* **446**, 937–940 (2007).
21. Xu, J. *et al*. Microfabricated "Biomolecular Ink Cartridges"—surface patterning tools (SPTs) for the printing of multiplexed biomolecular arrays. *Sens. Actuators B Chem.* **113**, 1034–1041 (2006).
22. Weber, R.J., Liang, S.I., Selden, N.S., Desai, T.A. & Gartner, Z.J. Efficient targeting of fatty-acid modified oligonucleotides to live cell membranes through stepwise assembly. *Biomacromolecules* **15**, 4621–4626 (2014).
23. Debnath, J., Muthuswamy, S.K. & Brugge, J.S. Morphogenesis and oncogenesis of MCF-10A mammary epithelial acini grown in three-dimensional basement membrane cultures. *Methods* **30**, 256–268 (2003).
24. Nguyen-Ngoc, K.-V. *et al*. ECM microenvironment regulates collective migration and local dissemination in normal and malignant mammary epithelium. *Proc. Natl. Acad. Sci. USA* **109**, E2595–E2604 (2012).
25. Laird, A.K. Dynamics of tumor growth. *Br. J. Cancer* **13**, 490–502 (1964).
26. Chi, X. *et al*. Ret-dependent cell rearrangements in the Wolffian duct epithelium initiate ureteric bud morphogenesis. *Dev. Cell* **17**, 199–209 (2009).
27. Lecaudey, V., Cakan-Akdogan, G., Norton, W.H.J. & Gilmour, D. Dynamic Fgf signaling couples morphogenesis and migration in the zebrafish lateral line primordium. *Development* **135**, 2695–2705 (2008).
28. Ghabrial, A.S. & Krasnow, M.A. Social interactions among epithelial cells during tracheal branching morphogenesis. *Nature* **441**, 746–749 (2006).
29. Shaw, A.T. *et al*. Sprouty-2 regulates oncogenic K-ras in lung development and tumorigenesis. *Genes Dev.* **21**, 694–707 (2007).
30. Slattum, G., Gu, Y., Sabbadini, R. & Rosenblatt, J. Autophagy in oncogenic K-Ras promotes basal extrusion of epithelial cells by degrading S1P. *Curr. Biol.* **24**, 19–28 (2014).
31. Chung, K. *et al*. Structural and molecular interrogation of intact biological systems. *Nature* **497**, 332–337 (2013).
32. Jain, R.K. Molecular regulation of vessel maturation. *Nat. Med.* **9**, 685–693 (2003).
33. Bhatia, S.N. & Ingber, D.E. Microfluidic organs-on-chips. *Nat. Biotechnol.* **32**, 760–772 (2014).
34. Yang, J. *et al*. Reconstruction of functional tissues with cell sheet engineering. *Biomaterials* **28**, 5033–5043 (2007).
35. L'Heureux, N., Pâquet, S., Labbé, R., Germain, L. & Auger, F.A. A completely biological tissue-engineered human blood vessel. *FASEB J.* **12**, 47–56 (1998).

ONLINE METHODS

General materials and reagents. Aldehyde-silanized glass slides (Nexterion Aldehyde AL, Schott), Sigmacote (Sigma-Aldrich), Sylgard 184 (Fisher Scientific), sodium borohydride ($NaBH_4$, ACROS, 98%), Pluronic F108 NF (BASF), ethanol (Fisher Scientific), trypsin inhibitor from Glycine max (Sigma-Aldrich), Matrigel (BD Biosciences), rat-tail collagen 1 (BD Biosciences), Turbo DNase (Life Technologies), amine-modified ssDNA (5′-amine-X_{20}, Operon), PBS (UCSF Cell-Culture Facility), PBS-CMF (UCSF Cell-Culture Facility), trypsin (UCSF Cell-Culture Facility), 100× penicillin-streptomycin, heat-inactivated FBS (UCSF Cell-Culture Facility), and RPMI medium (UCSF Cell-Culture Facility) were used as received without further purification. Lipid-modified ssDNA (5′-lipid-T_{80}-X_{20}) was synthesized as previously described[17].

Cell culture. MCF10A and MCF10AT cell lines were obtained from the Barbara Ann Karamanos Cancer Institute. Finite-lifespan HMECs and fibroblasts were provided by J.C.G. HUVECs, MSCs, and SMCs were purchased from Lonza. HBVPs were purchased from Sciencell. CAD cells were provided by K. Monahan. Bone marrow dendritic cells were provided by B. Boldajipour. Jurkats were purchased from the American Type Culture Collection.

MCF10A and MCF10AT cell lines were cultured as previously described[23,36]. Primary human mammary epithelial cells at passage 4 were established and maintained in M87A medium according as previously described[37]. CAD neuronal cells were cultured as previously described[38]. All other cells were cultured according to standard practices listed on American Type Culture Collection or Lonza.

No mycoplasma testing or cell authentication was performed for the experiments in this study.

Antibodies. For immunofluorescence, the following antibodies were used: anti-human keratin 19 (Sigma cat. #C6930) (clone A53-B/A2) (1:50 dilution), anti-human keratin 14 (Thermo cat. #RB-9020-P) (polyclonal) (1:50 dilution), and anti-human CD49f (Millipore cat. #MAB1378) (clone GoH3) (1:50 dilution).

Preparation of PDMS flow cells. Flow cells were cast with Sylgard 184 according to the specifications provided by Dow Corning. Briefly, the polymer and curing agent were mixed at a 10:1 ratio, degassed under vacuum, and cured over the flow-cell master at 70 °C. The master was prepared with no. 1–thickness coverslips (Fisher Scientific) cut to the dimensions of 4.5 mm × 18 mm and attached to double-sided tape (3M, cat. 665) of 0.0762-μm thickness. The final dimensions of the flow-cell master were 4.5 mm × 18 mm × 0.22 mm attached to a Nunclon (Fisher Scientific) Petri dish. Each PDMS flow cell was individually cut to have 1-mm-thick side walls and to have a 4.5-mm-wide inlet and outlet. Flow cells were treated with atmospheric plasma before use, as described below.

Preparation of DNA-patterned surfaces. Cell and tissue patterns were designed as bitmap images in Microsoft Paint and translated into 6- to 8-μm-diameter droplets of 1.5 mM 5′-amine-modified ssDNA (5′-amine-X_{20}, Operon) in a spotting solution of 225 mM NaCl, 22.5 mM sodium citrate, 5% (w/v) trehalose, 0.1 mg ml^{-1} N-octylglucoside, pH 9.5, onto aldehyde-silanized glass slides (Nexterion Aldehyde AL, Schott) via the BioForce Nano eNabler. Upon completion of printing, ssDNA patterns were baked at 120 °C for 15 min and then stored in a vacuum desiccator until use.

Patterned slides were reduced in a solution of 0.25% $NaBH_4$ in 25% ethanol and 75% PBS for 15 min. Slides were washed twice with 0.1% SDS, washed three times with dH_2O, and then air-dried. For silanization, 150 μl of Sigmacote (Sigma-Aldrich) were pipetted onto the slide and a coverslip placed on top. After 5 s, the coverslip was removed and the slide submerged into a tube of 50 ml absolute ethanol. The slide was inverted ten times and then transferred into a fresh tube of 50 ml absolute ethanol. The inverting was repeated, and the slide was transferred into a tube of dH_2O for a final set of inversions. The slide was removed from the tube and dried under a stream of air. A flow cell was cut for each pattern on the slide, cleaned of dust with tape, and subjected to atmospheric plasma in a Plasma Etch PE-50 for 35 s under 200-mtorr pressure with 15 cc min^{-1} gas flow and at intermediate power. Flow cells were immediately positioned over the patterned slide and secured with gentle finger pressure. The flow cells were primed with a solution of RPMI-1640, 10% FBS, 63.7 mg l^{-1} penicillin G, 100 mg l^{-1} streptomycin sulfate, and 1% Pluronic F108. The solution was left in the flow cell for 5 min at room temperature to block the surface, and then the flow cell was equilibrated with four flow-cell volumes of calcium- and magnesium-free PBS (PBS CMF) and left undisturbed until ready for programmed assembly.

Preparation of DNA-labeled cells. All cell-lines were labeled with lipid-ssDNA prepared according to a published procedure[1]. Briefly, cells were incubated for 5 min at room temperature with 5 μM of lipid-DNA. Sequences were chosen according to the requirements of each specific experiment. DNA-labeled cells were washed three times with PBS CMF and temporarily stored on ice until required for programmed assembly. DNA sequences are provided in **Supplementary Table 2**.

Programmed assembly and tissue embedding of cell patterns. DNA-labeled cells were resuspended to a concentration of 10^7 cells ml^{-1}, and 20 μl of this suspension were introduced to one end of the flow cell. Either the cells were allowed to settle to the surface by gravity for 5–10 min or the slide was centrifuged for 3 min at 8g in a Sorvall Legend RT+ centrifuge with acceleration and deceleration set to minimum. Ten flow-cell volumes of PBS CMF were introduced into the flow cell to wash out unhybridized cells. The procedures in this paragraph were repeated for each assembly step desired, taking 5–15 min for each successive assembly step.

Once the desired cell populations were assembled in the flow cell, a mixture of hydrogel precursor (for example, Matrigel) and DNase was introduced to the flow cell. One typical formulation was 6.1 mg ml^{-1} Matrigel, 2.1 mg ml^{-1} collagen I, 40 U ml^{-1} Turbo DNase, ice cold. Another typical formulation was 9.0 mg ml^{-1} Matrigel, 40 U ml^{-1} Turbo DNase, ice cold. The flow cell was put in an incubator at 37 °C for 30 min to allow for DNA cleavage and for the liquid gel to set as a solid hydrogel. Next, a border of 20 μl PBS CMF was applied all around the flow cell to reduce stiction, and then a sterile razor blade was used to slide the flow cell off the surface and onto a 20-μl droplet of hydrogel precursor

waiting in a 3.5-cm culture dish. The dish was transferred to an incubator at 37 °C for 30 min to allow the underlying gel to set. 3 ml of prewarmed culture medium were added to the dish so as to completely submerge the flow cell. Sharp tweezers were used to carefully slide the flow cell off the set hydrogel. The released flow cell was then removed from the dish. The dish was returned to the incubator for culture.

Immunofluorescence. All samples were fixed with 4% formaldehyde for 20 min and then incubated in blocking buffer (10% heat-inactivated goat serum in PBS+0.5% Triton X-100) at 4 °C for at least 1 d. Primary antibodies were then diluted in blocking buffer and added to the sample. After at least 1 d incubating at 4 °C with the primary antibodies, samples were washed several times with PBS+Triton X-100 for at least one day and incubated with fluorophore-conjugated secondary antibodies diluted at a concentration of 1:200 in blocking buffer for approximately 1 d. All sample were washed with PBS+1 μg ml^{-1} DAPI for at least 1 h before imaging.

Image acquisition. All confocal microscopy images were acquired using a temperature-, atmosphere-, and humidity-controlled spinning-disk confocal microscope (Zeiss Cell Observer Z1 equipped with a Yokagawa spinning disk and running Zeiss Zen Software). All other images were acquired using an inverted epifluorescence microscope (Zeiss Axiovert 200M running SlideBook software).

Cell growth measurements. Cell assemblies in 20×20 square arrays with pitch xy of 300 μm were imaged approximately every 24 h by driving the Zeiss Cell Observer spinning-disk confocal microscope to a preset list of nominal xy positions at 20× magnification with a z-slice spacing of 3 μm. Cell nuclei in red and green emission channels were counted manually from raw .tiff z stacks and maximum-intensity projection images. Growth rates for each assembly were calculated as the slope of plots of $\log_2(N/N_o)$ vs. t where N is cell number at time t and N_o is initial cell number, assuming logarithmic growth of cells.

36. Dawson, P.J., Wolman, S.R., Tait, L., Heppner, G.H. & Miller, F.R. MCF10AT: a model for the evolution of cancer from proliferative breast disease. *Am. J. Pathol.* **148**, 313–319 (1996).
37. Stampfer, M.R., LaBarge, M.A. & Garbe, J.C. in *Cell and Molecular Biology of Breast Cancer* (ed. Schatten, H.) Ch. 15, 323–361 (Humana, 2013).
38. Qi, Y., Wang, J.K.T., McMillian, M. & Chikaraishi, D.M. Characterization of a CNS cell line, CAD, in which morphological differentiation is initiated by serum deprivation. *J. Neurosci.* **17**, 1217–1225 (1997).